JOURNAL OF GUIDANCE, CONTROL, AND DYNAMICS
Vol. 39, No. 3, March 2016

Engineering Notes

Novel Active Tuned Mass Damper Control Method for Space Telescope

Zhenbang Xu,* Jianfeng Yang,† Yingying Gu,‡ Qingwen Wu,§ Zhitao Luo,¶ and Hongwei Liu**
Changchun Institute of Optics, Fine Mechanics and Physics, Chinese Academy of Sciences, 130033 Changchun, People's Republic of China

DOI: 10.2514/1.G001509

I. Introduction

THE tuned mass damper (TMD) suppresses structural vibration responses by improving the damping performance of the primary vibration system. This apparatus has been applied successfully to vehicles [1], aircraft [2], buildings [3,4], and spacecraft [5].

With the development of space technology, the demands for the stability of space telescopes [6], such as the James Webb Space Telescope with pointing stability of 0.004 arc sec [7], the Space Interferometry Mission [8], and the Terrestrial Planet Finder [9], are becoming increasingly prominent. As an effective vibration attenuation apparatus, the TMD has been applied to improve image stability and the performance of space telescopes, e.g., Camelo and Adamm et al. used the TMD with variable damping and frequency to improve the surface accuracy of a segmented mirror of a large space mirror [10,11]. Compared with the passive TMD, the active TMD (ATMD) is more suitable for applications in space because of its smaller mass and volume.

The control strategy of the ATMD is an important factor of the performance of the ATMD. Many control strategies have been researched, including pole placement [12,13], state parameter feedback [14,15], positive position feedback (PPF) [16,17], and time-delay feedback [18]. PPF is an effective control strategy for vibration active control and has been extensively adopted for its advantages of good stability and low energy requirements [19–24], e.g., the NASA/DLR Stratospheric Observatory for Infrared Astronomy used multiple ATMDs with PPF to suppress structural flexible resonance at 37 and 75 Hz [16], Cohan and Miller used PPF to control the dynamic wavefront for lightweight mirrors of a space telescope [23], and de Marneffe et al. developed a six-axis vibration isolation system for a space application with PPF [21]. The application of PPF to an ATMD requires a compensator, which is designed according to the dynamic parameters of the actuators, to ensure stability [17,25]. Consequently, the variation in the dynamic parameters of the actuator in use may affect the vibration attenuation and stability of the ATMD, which restricts the application of the ATMD to a space device requiring high stability, such as a space telescope.

The dynamic-response amplitude–frequency curve of the primary system with and without the ATMD is usually used to access the vibration attenuation effect [26,27]. The basic objective of applying an ATMD to the optical payload is to improve the image quality of the optical system. Therefore, not only the amplitude-frequency curve but also the integrated optomechanical analysis [28,29] is required to evaluate the vibration attenuation effect of the ATMD.

The present study proposes a novel control strategy of the ATMD that consists of proportional control and PPF. The strategy has the advantages of good stability and independence from dynamic parameters of the ATMD and is thus suited to space devices. To solve the low-frequency resonance problem of the space telescope caused by vibration isolators, ATMDs with the developed control strategy are applied, and an integrated optomechatronics analysis is carried out to verify the vibration attenuation effect of the presented method.

The note is organized as follows. Section II describes the ATMD control strategy for a single-degree-of-freedom system and multi-degree-of-freedom system in detail. Section III presents the integrated optomechatronics simulation approach and simulation results. Concluding remarks on the ATMD are presented in Sec. IV.

II. Control Strategy of the Active Tuned Mass Damper

A. Control Strategy for a Single-Degree-of-Freedom System

The ideal PPF force control system for a single degree of freedom is depicted in Fig. 1. The primary vibration system consists of a lumped mass and a soft spring k in parallel with the damping c. An accelerometer is placed on the mass. The control force F_{ideal} is calculated with the PPF controller and is exerted on the mass directly. F_{ideal} can be expressed as

$$F_{\text{ideal}} = G(s)\ddot{x}_p \tag{1}$$

where $G(s)$ is the transmission function of the PPF controller and is expressed as [30]

$$G(s) = \frac{-g}{s^2 + 2\xi_f\omega_f s + \omega_f^2} \tag{2}$$

with ξ_f and ω_f being the damping and filter frequency of the controller, respectively. As shown in Eq. (2), the parameters of the PPF control are g, ξ_f, and ω_f.

For the ideal PPF force control system, the gain g of the PPF can be very large, and consequently large active damping can be achieved. For the practical control system with the ATMD, the dynamic characteristics of the actuator of the ATMD may affect the stability and performance. The common configuration of the practical control system with the ATMD dynamics is presented in Fig. 2. In this configuration, the ATMD is usually used as an inertial actuator whose natural frequency is lower than the target frequency band. Constrained by the dynamic characteristic of the ATMD, the gain g of the PPF controller cannot be as large as the ideal PPF force control, or the system will become unstable. Moreover, the system may also be

Received 2 June 2015; revision received 8 June 2015; accepted for publication 18 September 2015; published online 14 December 2015.

*Associate Researcher, Innovation Lab of Space Robot System, Space Robotics Engineering Center, Changchun Institute of Optics, Fine Mechanics and Physics, No. 3888 Dong Nanhu Road; xuzhenbang@gmail.com.

†Ph.D. Candidate, University of Chinese Academy of Sciences, No. 19A Yuquan Road, 100049 Beijing, People's Republic of China; yangjeff2013@163.com.

‡Research Assistant, Innovation Lab of Space Robot System, Space Robotics Engineering Center, Changchun Institute of Optics, Fine Mechanics and Physics, No. 3888 Dong Nanhu Road; 18686681605@163.com.

§Researcher, Space Robotics Engineering Center, Changchun Institute of Optics, Fine Mechanics and Physics, No. 3888 Dong Nanhu Road; wuqw@ciomp.ac.cn.

¶Research Assistant, Space Robotics Engineering Center, Changchun Institute of Optics, Fine Mechanics and Physics, No. 3888 Dong Nanhu Road; 41373931@qq.com.

**Associate Researcher, Space Robotics Engineering Center, Changchun Institute of Optics, Fine Mechanics and Physics, No. 3888 Dong Nanhu Road; liuhw@ciomp.ac.cn.

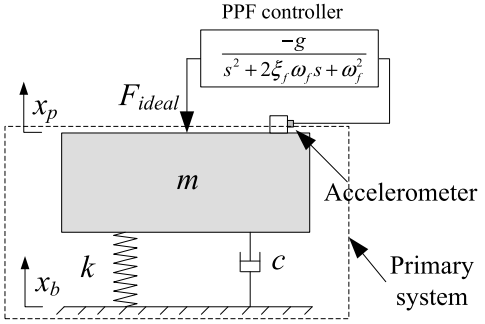

Fig. 1 Schematic diagram of the ideal PPF force control system.

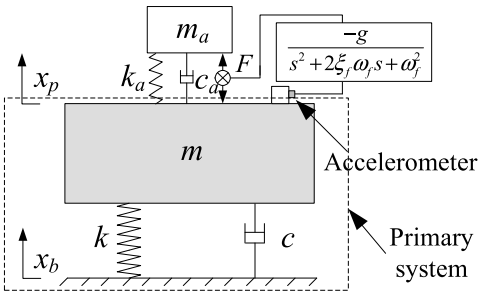

Fig. 2 Schematic diagram of the practice PPF controller system considering the dynamic characteristic of the inertial actuator.

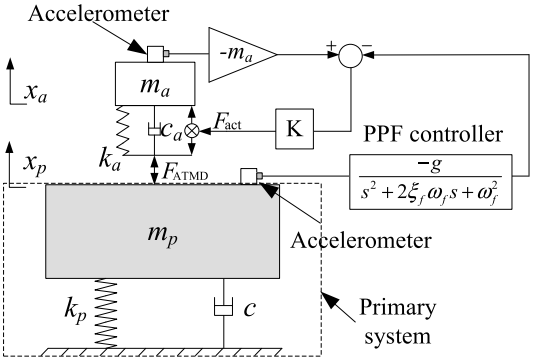

Fig. 3 Schematic diagram of the developed PPF controller system.

unstable in the case that the damping of the ATMD c_a is very small [31]. To ensure the stability and performance of the ATMD, the control system requires a compensator, which is designed according to the dynamic characteristic of the ATMD. Because the performance depends very much on the accuracy of dynamic parameters, the variation of the dynamical parameters of the ATMD in use strongly affects the compensation effect.

To solve the problems stated previously, a novel control strategy is proposed as shown in Fig. 3. In this control strategy, an added accelerometer is attached to the mass of the ATMD. In Fig. 3, x_p is the displacement of the primary system, and x_a is the displacement of the ATMD.

According to Newton's second law, the active force exerted at the primary system can be written as

$$F_{\text{ATMD}} = -m_a \ddot{x}_a \tag{3}$$

From Eq. (3), it is clear that the force F_{ATMD} is proportional to the acceleration of the mass m_a, and the active force may thus be controlled by controlling the acceleration of the mass m_a.

To ensure F_{ATMD} is equal to F_{ideal}, proportional control is adopted. The difference between the active force F_{ATMD} and the ideal feedback force F_{ideal} is taken as the error signal. The error signal is amplified through the proportional controller and transferred as a control signal to drive the actuator:

$$F_{\text{act}} = K(F_{\text{ATMD}} - F_{\text{ideal}}) \tag{4}$$

where K is the gain of the proportional controller.

In essence, this practical control system implementing the proposed strategy is equivalent to the ideal PPF force control. It has the advantage that the system performance is independent of the actuator characteristic. As a result, the stability and performance of the control system are unaffected by the variation of the dynamic characteristics of the ATMD.

To validate the effectiveness of the control strategy, simulations are carried out using the model shown in Fig. 3. Table 1 gives the specifications of the primary system. Table 2 gives the parameters of the ATMD in different cases.

Figure 4 compares the root loci of the gain K of the proportional controller in different cases. It is seen that the ATMD dynamics affect the positions of the closed poles. The closed-loop poles of the ATMDs in different cases converge to the same position as the gain g tends to infinity, and the finally positions of the closed-loop poles are the same as those of the ideal PPF force control. As shown in Fig. 4, when the gain g is greater than 12, the closed-loop poles are extremely close to the final position in case 1, and the gain K in cases 2 and 3 are 23 and 36, respectively. It demonstrates that the closed poles of the ATMD with low natural frequency move much more quickly, and a further increase in gain K does not strongly affect the performance of the system.

When the K varies from 0 to ∞, the root locus may be in the right half-plane. However, as the K increases, the root locus moves back to the left half-plane and keeps the system stability. Figure 4 shows that larger K is needed to keep stability when the natural frequency of the actuator is higher. In this simulation, the stability of the system can be achieved when the gain K is greater than 94.6 in case 3.

Figure 5 shows the transmissibility curves of the primary mass with and without ATMDs. It is seen that the vibration attenuation effects of the ATMDs with different dynamic characteristics are identical, which indicates that the inherent dynamic characteristics of the ATMD can be ignored using the proposed control strategy. In addition, the ATMD with the proposed control strategy can achieve the same attenuation effect as the ideal PPF force control.

B. Control Strategy for a Multi-Degree-of-Freedom System

The sensitive payloads are almost a continuous flexible structure in practice, especially for a space telescope. Thus, in practical applications, multiple ATMDs are required to achieve the effect of mitigation vibration. If we approximate the payload structure as having a finite number of degrees of freedom, we can formulate a transformation between physical and modal coordinates. A control strategy based on the modal space is adopted in this study as shown in Fig. 6.

The modal coordinate matrix obtained by analysis or measurement may be described as

Table 1 Specifications of the primary system

Notation	Specification	Value
m_p	Mass of the primary system	100 kg
f_p	Natural frequency of the primary system	20 Hz
c_p	Viscous damping coefficient of primary damper	753.6 N/(m · s^{-1})
ξ_p	Damping ration of the sensitive payload	0.03

Table 2 Parameters of the ATMD in different cases

		Value		
Notation	Specification	Case 1	Case 2	Case 3
m_a	Mass of the actuator, kg	5	5	5
f_a	Natural frequency of the actuator, Hz	10	20	30
c_a	Viscous damping coefficient of the second damper, N/(m · s^{-1})	6.28	12.56	18.84
ξ_a	Damping ration of the actuator	0.01	0.01	0.01

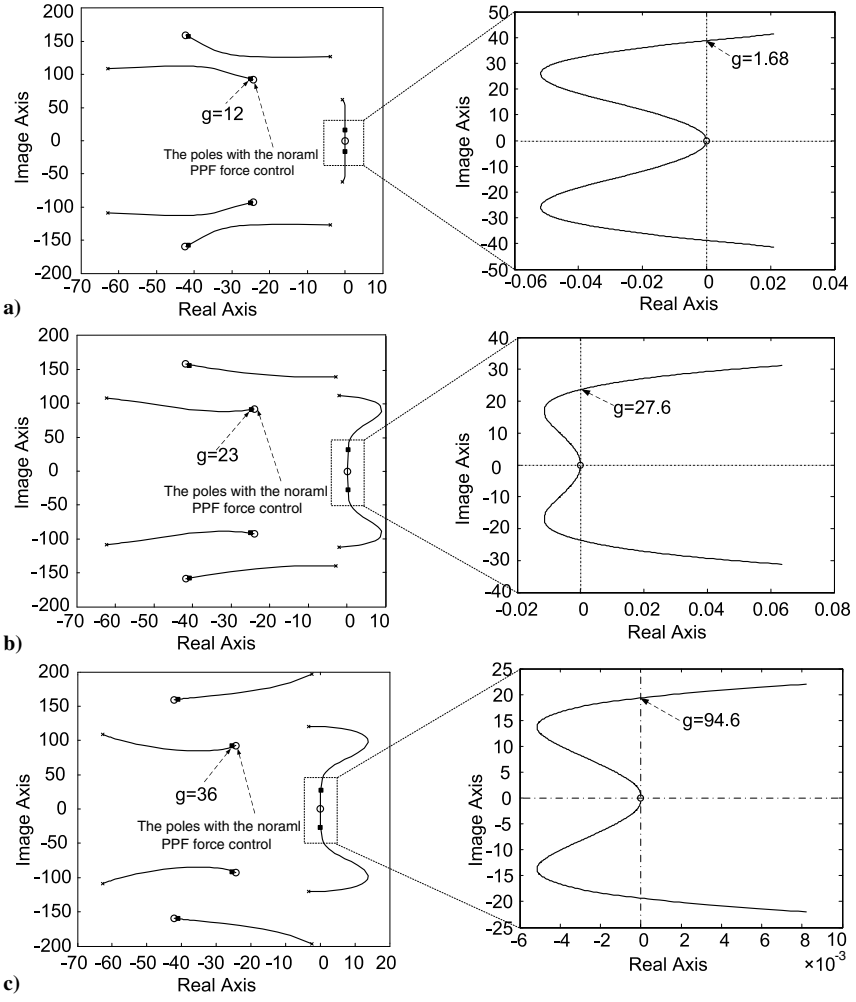

Fig. 4 Root locus of the control system in different cases: a) case 1, b) case 2, and c) case 3.

$$[\Phi_{\text{tot}}] = [\phi_1 \quad \phi_2 \quad \cdots \quad \phi_n] \tag{5}$$

where $[\Phi_{\text{tot}}]$ is the $\boldsymbol{n} \times \boldsymbol{n}$ eigenvector matrix of $[\boldsymbol{M}^{-1}][\boldsymbol{K}]$ and denotes the first n modes, and ϕ_n is the $\boldsymbol{n} \times 1$ vector of the nth-order mode.

The coordinate change from physical space to modal space is

$$\boldsymbol{a}_{\text{mod}} = [\Phi_{\text{tot}}]^T \boldsymbol{a} \tag{6}$$

where $\boldsymbol{a}_{\text{mod}}$ is an $\boldsymbol{n} \times 1$ vector containing all the system physical coordinates, $\boldsymbol{a}$ is an $\boldsymbol{n} \times 1$ vector containing all the system physical coordinates and can be measured by accelerometers, and $[\Phi_{\text{tot}}]^T$ is the transpose of the modal coordinate matrix $[\Phi_{\text{tot}}]$.

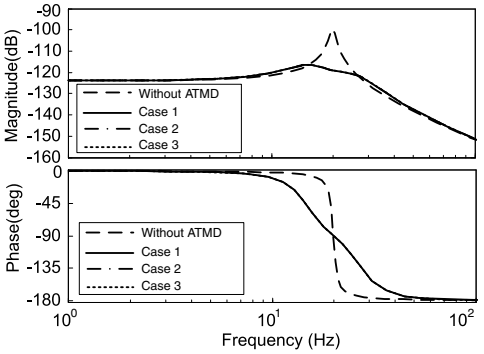

Fig. 5 Transmissibility curves of the primary system without and with different ATMDs.

Employing a modal coordinate transformation, the multi-degree-of-freedom coupling system can be converted to a series of decoupled scalar systems. Therefore, the control system can be designed according to the single-degree-of-freedom control system described previously. The mode controller can be described as

$$\boldsymbol{G}(s) = \begin{bmatrix} G_1(s) & 0 & \cdots & 0 \\ 0 & G_2(s) & \cdots & 0 \\ \vdots & \vdots & \ddots & 0 \\ 0 & 0 & 0 & G_n(s) \end{bmatrix} \tag{7}$$

where $G_n(s)$ is the controller used for the nth-order mode.

The control forces in the modal coordinate system can be described as

$$\boldsymbol{F}_{\text{mod}} = \boldsymbol{G}(s)\boldsymbol{a}_{\text{mod}} \tag{8}$$

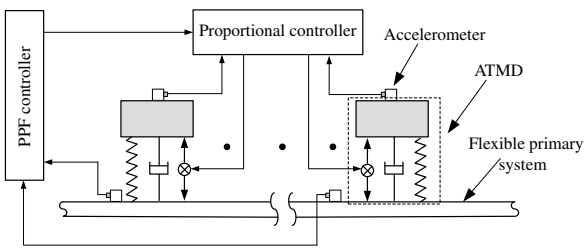

Fig. 6 Schematic diagram of the multi-degree-of-freedom control system.

Transforming the control forces from a modal coordinate system to a physical coordinate system, the control forces in the physical coordinate system can be derived as

$$\boldsymbol{F}_{\text{PPF}} = [\Phi_{\text{tot}}]\boldsymbol{F}_{\text{mod}} = [\Phi_{\text{tot}}]\boldsymbol{G}(s)[\Phi_{\text{tot}}]^T\boldsymbol{a} \tag{9}$$

Using the previous formulas, the PPF active forces may be obtained. Assigning the PPF active forces to each independent proportional controller of the ATMD, the practical active forces can be described by

$$\boldsymbol{F}_{\text{act}} = \boldsymbol{K}(-\boldsymbol{M}\boldsymbol{a} - \boldsymbol{F}_{\text{PPF}}) \tag{10}$$

where $\boldsymbol{M} = \text{diag}([\,m_1 \quad m_2 \quad \dots \quad m_n\,])$ is an $\boldsymbol{n} \times \boldsymbol{n}$ diagonal matrix consisting of mass parameters of multiple actuators, $\boldsymbol{a} = [\,a_1 \quad a_2 \quad \cdots \quad a_n\,]^T$ is the $\boldsymbol{n} \times 1$ vector of the acceleration of actuators, and $\boldsymbol{K} = \text{diag}([\,k_1 \quad k_2 \quad \cdots \quad k_n\,])$ is the diagonal matrix of the gain.

III. Integrated Optomechatronics Analysis

In response to the demands of space science missions, there are many very precise optical instruments in space telescopes. Such optical payloads are very sensitive to pointing disturbances. The dynamic perturbations of optical mirrors and detectors can notably degrade image quality. To meet the requirements of high pointing stability, vibration isolators are usually inserted in the transmission path between the disturbance source [32] and payload. A vibration isolation system was proposed and the way to obtain the optimal design parameters and configuration of the isolation system was discussed in [33]. However, vibration isolators lead to system resonance at the corner frequency, which cannot be solved by optimizing the design parameters and configuration. The general solution to this problem is to increase the damping of the isolators. However, the increasing damping affects the isolation effect of the isolators at high frequency. One effective approach used to solve this problem is to adopt ATMDs.

The telescope considered in this note is a classic Cassegrain system with a parabolic primary mirror and a hyperbolic secondary mirror.

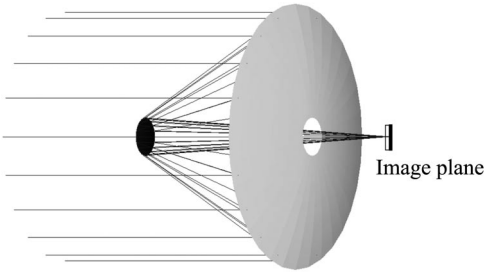

Fig. 7 Optical layout of a telescope.

Table 3 Natural frequencies and mode shapes

Mode	Natural frequency, Hz	Mode shape
First	9.7	Tilting around the y axis
Second	9.7	Tilting around the x axis
Third	16.5	Piston along the z axis
Fourth	17.1	Rolling around the y axis
Fifth	17.1	Rolling around the x axis
Sixth	19.6	Twisting around the z axis

The optical layout of the telescope studied in this research is depicted in Fig. 7. Figure 8 is the finite-element drawing of this approach. The architecture of the isolation system is based on the Stewart–Gough configuration, which consists of six isolation struts. Six ATMDs are attached at the upper end and along the axis of each strut. With this configuration, the ATMDs can attenuate effectively six resonant modes of the system.

To verify the effectiveness of this method in improving the image quality of the optical system, integrated optomechatronics analysis that predicts the jitter performance of the optical system is adopted. This integrated simulation combines the optical payload, isolation system, and ATMDs using the transmission function. The jitter performance of the optical system is defined as the line-of-sight (LOS) motion measured at the detector plane. For flexible optics, the microvibration may change the shape of the optical surfaces, and it is thus important to account for the deformations of the optical surfaces. The average rigid-body motions can be calculated using interpolation elements (RBE3 in Nastran) [34] or linear equations as follows.

The fit displacement of node i due to the motions is

$$\begin{aligned} d\tilde{x}_i &= T_x + z_i R_y - y_i R_z \\ d\tilde{y}_i &= T_y - z_i R_x + x_i R_z \\ d\tilde{z}_i &= T_z + y_i R_x - x_i R_y \end{aligned} \tag{11}$$

where $d\tilde{x}_i$, $d\tilde{y}_i$, $d\tilde{z}_i$ are respectively the displacements at node position x_i, y_i, z_i due to rigid-body motions; T_x, T_y, and T_z are the translations along the coordinate axes; and R_x, R_y, and R_z are the rotations about coordinate axes.

The error E is defined as the difference between the actual optical surface nodal displacements and the rigid-body values calculated previously:

$$E = \sum_{i=1}^{n} (w_i(dx_i - d\tilde{x}_i)^2 + w_i(dy_i - d\tilde{y}_i)^2 + w_i(dz_i - d\tilde{z}_i)^2) \tag{12}$$

where w_i is the weighting function of node i.

Taking partial derivatives with respect to each term (T_x, T_y, T_z, R_x, R_y, R_z) and setting the result to zero, the average rigid-body motions can be obtained as

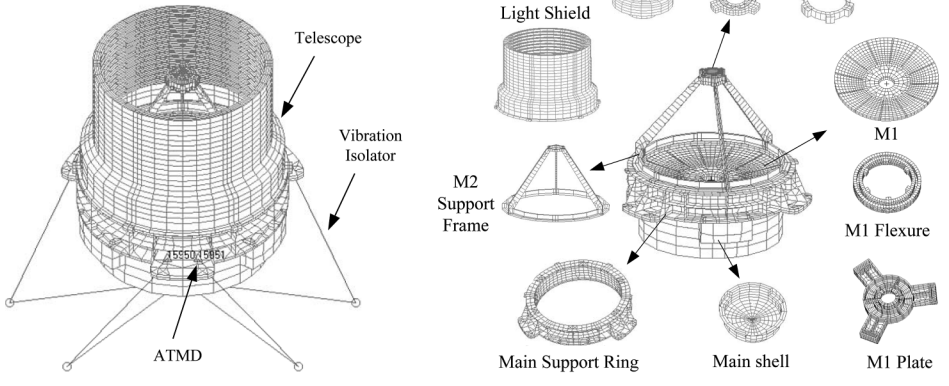

a) b)

Fig. 8 Structure of the optical payload: a) finite-element model, and b) explosive view of the FEM.

$$
\begin{cases}
\dfrac{\partial E}{\partial T_x} = \sum_{i=1}^{n} w_i[dx_i - (T_x + z_i R_y - y_i R_z)] = 0 \\
\dfrac{\partial E}{\partial T_y} = \sum_{i=1}^{n} w_i[dy_i - (T_y - z_i R_x + x_i R_z)] = 0 \\
\dfrac{\partial E}{\partial T_z} = \sum_{i=1}^{n} w_i[dz_i - (T_z + y_i R_x - x_i R_y)] = 0 \\
\dfrac{\partial E}{\partial R_x} = \sum_{i=1}^{n} w_i\{[dy_i - (T_y - z_i R_x + x_i R_z)]z_i - [dz_i - (T_z + y_i R_x - x_i R_y)]y_i\} = 0 \\
\dfrac{\partial E}{\partial R_y} = \sum_{i=1}^{n} w_i\{-[dx_i - (T_x + z_i R_y - y_i R_z)]z_i + [dz_i - (T_x + y_i R_x - x_i R_y)]x_i\} = 0 \\
\dfrac{\partial E}{\partial Z_z} = \sum_{i=1}^{n} w_i\{[dx_i - (T_x + z_i R_y - y_i R_z)]y_i - [dy_i - (T_y - z_i R_x + x_i R_z)]x_i\} = 0
\end{cases}
\tag{13}
$$

Substituting the nodal data of optical surfaces into Eq. (13) and solving these equations yields the average rigid-body motions (T_x, T_y, Tz, R_x, R_y, R_z). The average rigid-body motions can also be calculated by interpolation elements in MSC.NASTRAN software.

Image motion, as a function of time and frequency, can be computed from finite-element analysis. This method assumes that the image motion is a linear function of the optical element displacement [34,35]. The relationship of the image motion (Δx, Δy) and the average rigid-body motions ($[T]_{\text{optics}}$) can be expressed as

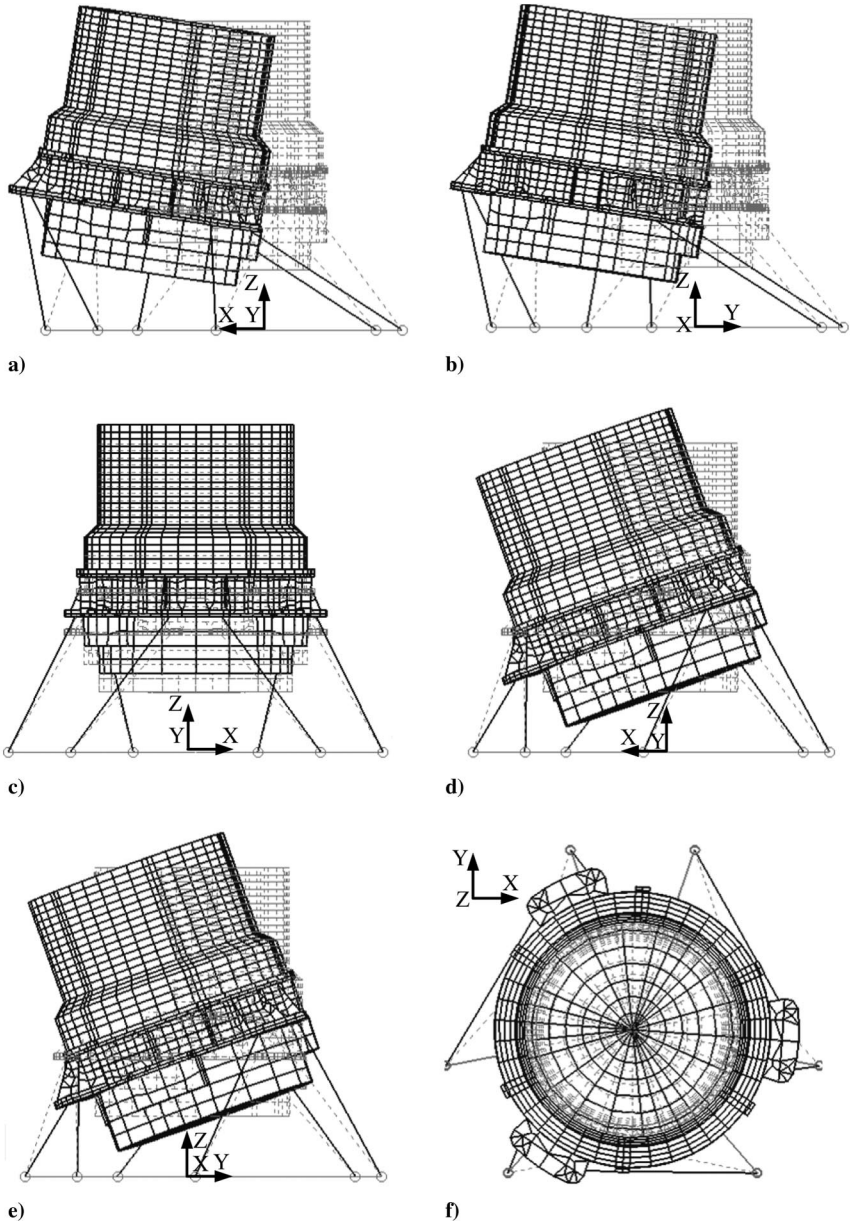

Fig. 9 Mode shapes of the first six modes of the isolation system.

Table 4 Six load cases for LOS jitter analysis

Load case	Acceleration	Frequency range, Hz
Translational vibration along the x axis	10^{-3} m/s^2	$1 \sim 5 \times 10^2$
Translational vibration along the y axis	10^{-3} m/s^2	$1 \sim 5 \times 10^2$
Rotational vibration around the x axis	10^{-3} arc/s^2	$1 \sim 5 \times 10^2$
Rotational vibration around the y axis	10^{-3} arc/s^2	$1 \sim 5 \times 10^2$
Translational vibration along the z axis	10^{-3} m/s^2	$1 \sim 5 \times 10^2$
Rotational vibration around the z axis	10^{-3} arc/s^2	$1 \sim 5 \times 10^2$

$$\begin{Bmatrix} \Delta x \\ \Delta y \end{Bmatrix} = [L]_{\text{img}}[T]_{\text{optics}} \tag{14}$$

where $[L]_{\text{img}}$ denotes optical sensitivity coefficients that can be obtained from an optical design code.

The dynamic equation of the system can be written as

$$[\boldsymbol{M}s^2 + \boldsymbol{B}s + \boldsymbol{K}]\{\boldsymbol{u}\} = \{\boldsymbol{P}\} \tag{15}$$

As stated previously, by employing the ATMD, it follows that

$$\boldsymbol{F}_{\text{act}} = \boldsymbol{g}(-\Phi \boldsymbol{G}(s)\Phi^T s^2 \boldsymbol{u}_d - \boldsymbol{M}s^2 \boldsymbol{u}_i) \tag{16}$$

where $\boldsymbol{u}_d$ is the 6×1 position vector of isolator mounting points, and $\boldsymbol{u}_i$ is the 6×1 displacement vector of the actuators. The transmission characteristics of the system in Eq. (14) can be added to Eq. (13) by adjusting the coefficient matrices $\boldsymbol{M}$, $\boldsymbol{B}$, and $\boldsymbol{K}$.

The first six natural frequencies and mode shapes of the system obtained employing the finite-element model (FEM) are given in Table 3 and Fig. 9 and are used to design the mode controller of the ATMDs.

To verify the effectiveness of the ATMDs in improving the image quality of the optical system, the LOS jitters of the optical system with and without ATMDs are calculated. Six load cases are considered. The cases are six disturbance accelerations applied to the base platform in six directions as shown in Table 4.

Figure 10 compares the LOS magnitudes of the optical system with and without the ATMDs in different cases. Figures 10a, 10b, and 10e show the translational vibration along the x axis, y axis, and z axis, respectively. Figures 10c, 10d, and 10f show the rotational vibration around the x axis, y axis, and z axis, respectively. It is seen that the ATMDs effectively suppress the resonant peaks of the isolation system, and moreover, the isolation effect of the isolation system at high frequency is unaffected. In this study, the gain g of the PPF is

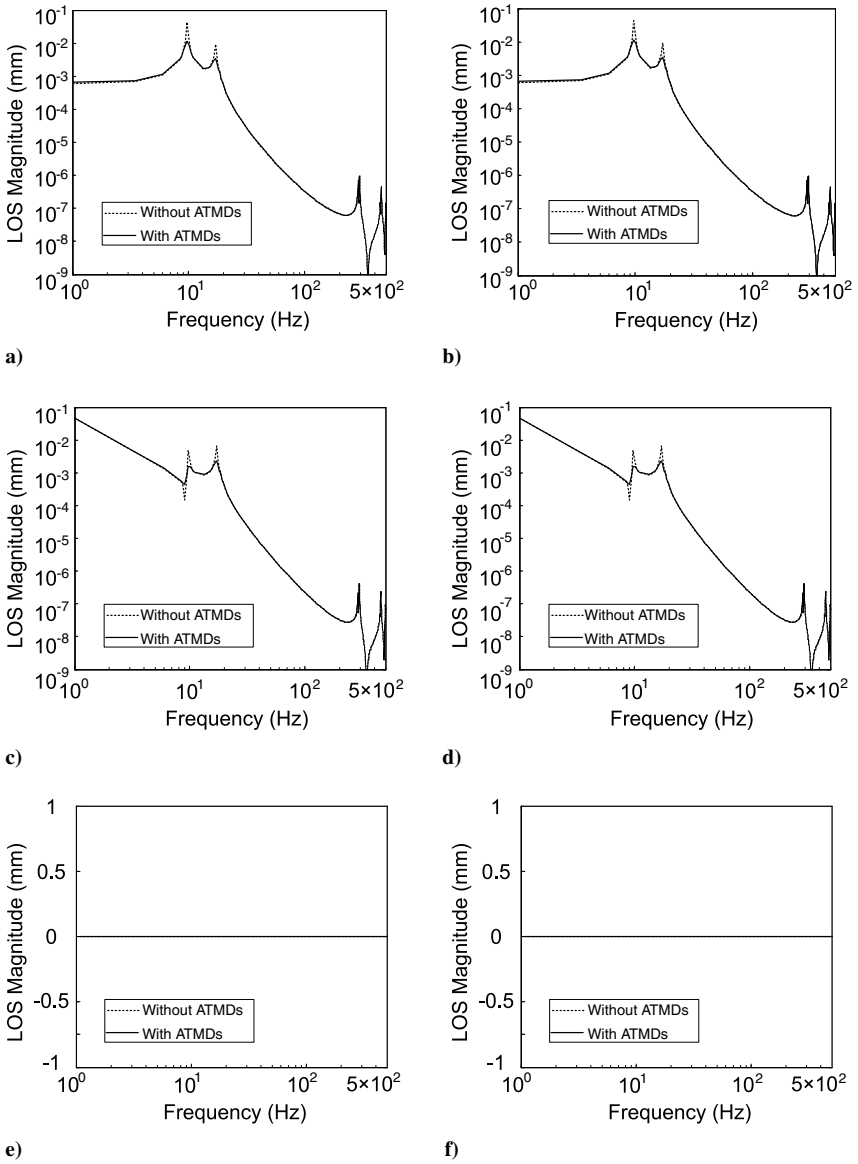

Fig. 10 Comparison of the LOS magnitude of the image with and without ATMDs in different cases.

Table 5 Natural frequencies and damping ratios of the closed-loop system

Natural frequencies without the ATMDs, Hz	Natural frequencies with the ATMDs, Hz	Damping ratio without the ATMDs	Damping ratio with the ATMDs	Increasing rate of damping ratio, %
9.7	9.7	0.0135	0.0722	535
9.7	9.7	0.0135	0.0722	535
16.5	16.5	0.0234	0.148	632
17.1	17.2	0.0238	0.0825	347
17.1	17.2	0.0238	0.0825	347
19.6	19.6	0.0273	0.154	564

120, and the vibration attenuation ratios at the resonant peaks are better than 10 dB. The peak attenuation is better with larger gain.

Because of the structural symmetry of the payload, the results in Figs. 10a and 10b are almost identical, as in the comparison of Figs. 10c and 10d and the comparison of Figs. 10e and 10f. There is less image motion in Figs. 10a and 10b than in Figs. 10c and 10d, which indicates that image motion on the detector is more sensitive to rotational vibration than to translational vibration.

The curves in Figs. 10c, 10d present a decreasing trend of the LOS magnitude with increasing frequency. This trend is due to the gradual decrease in disturbance displacement with the rise in frequency when the disturbance acceleration is invariable. Two peaks occur at low frequency because of the resonance of the isolation system. Other peaks occur at high frequency because of the elastic resonance of the support frame.

The LOS magnitudes of the image shown in Figs. 10e and 10f are constantly zero. Thus, the microvibrations along the z axis and around the z axis do not affect the optic axis direction and thus have no effect on the image quality of the optical system.

The natural frequencies and damping ratio of the system for different modes are calculated and the results presented in Table 5. It is seen that the natural frequencies of the optical payload with the ATMDs are not notably different from those without ATMDs. With the collocated configuration, the ATMDs can increase the damping of six modes of the system, especially in the z-axis direction, where the increase reaches 632%. The damping ratios of vibrations around the x axis and y axis increase less, by up to 347%.

IV. Conclusions

This study presented a novel active tuned mass damper (ATMD) control strategy and investigated the application of the ATMD to the vibration attenuation of a space telescope. This control strategy, which combines proportional control and positive position feedback (PPF), was shown to have good stability. Moreover, the control strategy is independent of the dynamic characteristics of the ATMD. The effectiveness of the presented control strategy was demonstrated in simulations. The simulation results show that the control strategy can achieve the same effect as ideal PPF force control. To verify the vibration attenuation effect of the developed ATMDs applied to the space telescope, an integrated optomechatronics analysis was adopted. The optomechatronics simulation results show that the ATMDs can efficiently attenuate the elastic resonance of the space telescope and improve the image quality of the optical system. In addition, the ATMDs do not reduce the isolation effect of the isolation system at high frequency ranges.

Acknowledgments

This work is supported by the National Natural Science Foundation of China under grant 11302222 and the Innovation Foundation of Changchun Institute of Optics, Fine Mechanics and Physics, Chinese Academy of Sciences under grant Y4CX1SS141.

References

[1] Liu, H. P., Wu, T. X., and Li, Z. G., "Theoretical Modeling and Effectiveness Study of Rail Vibration Absorber for Noise Control," *Journal of Sound and Vibration*, Vol. 38, Nos. 12, 2009, pp. 594–608. doi:10.1016/j.jsv.2009.01.036

[2] Oliver, A., Bauchau, J. R., and Chen, S. Y., "Modeling the Bifilar Pendulum Using Nonlinear, Flexible Multibody Dynamics," *Journal of the American Helicopter Society*, Vol. 48, No. 1, 2003, pp. 53–62. doi:10.4050/JAHS.48.53

[3] Nagarajaiah, S., Asce, M., and Sonmez, E., "Structures with Semiactive Variable Stiffness Single/Multiple Tuned Mass Dampers," *Journal of Structural Engineering*, Vol. 133, No. 1, 2007, pp. 67–77. doi:10.1061/(ASCE)0733-9445(2007)133:1(67)

[4] Li, L. Y., Song, G. B., Sigla, M., and Mo, Y. L., "Vibration Control of a Traffic Signal Pole Using a Pounding Tuned Mass Damper with Viscoelastic Materials (2): Experimental Verification," *Journal of Vibration and Control*, Vol. 21, No. 4, 2015, pp. 670–675. doi:10.1177/1077546313488407

[5] Ahmadi, G., Ellison, J. F., and Grodsinsky, C. M., "Vibration Control of Equipment Aboard Spacecraft," *Proceeding of the SPIE Active Materials and Smart Structures Conference*, Vol. 2427, SPIE, Bellingham, WA, 1994, pp. 80–92. doi:10.1117/12.200935

[6] Luo, Q., Li, D. X., and Zhou, W. Y., "Studies on Vibration Isolation for a Multiple Flywheel System in Variable Configurations," *Journal of Vibration and Control*, Vol. 21, No. 1, 2015, pp. 105–123. doi:10.1177/1077546313490005

[7] Bronowicki, A. J., "Vibration Isolator for Large Space Telescopes," *Journal of Spacecraft and Rockets*, Vol. 43, No. 1, 2006, pp. 45–53. doi:10.2514/1.12036

[8] Miller, D. W., de Weck, O. L., Uebelhart, S. A., Grogan, R., and Basdogan, I., "Integrated Dynamics and Controls Modeling for the Space Interferometry Mission (SIM)," *Proceedings of the 2001 IEEE Aerospace Conference*, Vol. 4, IEEE Publ., Piscataway, NJ, 2001, pp.2089–2102. doi:10.1109/AERO.2001.931545

[9] Liu, K. C., Blaurock, C., Alexander, J., and Dewell, L., "Terrestrial Planet Finder Coronagraph Pointing Control System Design and Evaluation for Flight Baseline 1," *Proceeding of the SPIE Optical Modeling and Performance Predictions II Conference*, Vol. 5867, SPIE, Bellingham, WA, 2005, Paper 58670Z.

[10] Camelo, V., Bronowicki, A., Simonian, S., Hejal, R., and Brennan, S., "Damping and Isolation Concepts for Vibration Suppression and Pointing Performance," *50th AIAA/ASME/ASCE/AHS/ASC Structures, Structural Dynamics, and Materials Conference*, AIAA Paper 2009-2637, May 2009.

[11] Adamm, J. Y., and Briji, N. A., "Applications of Tuned Mass Dampers to Improve Performance of Large Space Mirrors," *Acta Astronautica*, Vol. 94, No. 1, 2014, pp. 1–13. doi:10.1016/j.actaastro.2013.07.039

[12] Lee, K. Y., and Renshaw, A. A., "Eigenvalue Estimation Using Linearly Dependent Eigenfunctions," *Journal of Vibration and Acoustics*, Vol. 122, No. 4, 2000, pp. 464–469. doi:10.1115/1.1310327

[13] Bisegna, P., and Caruso, G., "Closed-Form Formulas for the Optimal Pole-Based Design of Tuned Mass Dampers," *Journal of Sound and Vibration*, Vol. 331, No. 10, 2012, pp. 2291–2314. doi:10.1016/j.jsv.2012.01.005

[14] Chatterjee, S., "On the Efficacy of an Active Absorber with Internal State Feedback for Controlling Self-Excited Oscillations," *Journal of Sound and Vibration*, Vol. 330, No. 7, 2011, pp. 1285–1299. doi:10.1016/j.jsv.2010.10.011

[15] Nagashima, I., "Optimal Displacement Feedback Control Law for Active Tuned Mass Damper," *Earthquake Engineering and Structural Dynamics*, Vol. 30, No. 8, 2001, pp. 1221–1242. doi:10.1002/eqe.60

[16] Keas, P. J., Dunham, E., Lampater, U., Pfuller, E., and Teufel, S., "Active Damping of the SOFIA Telescope Assembly," *Proceeding of the SPIE Ground-Based and Airborne Telescopes IV Conference*, Vol. 8444, SPIE, Bellingham, WA, July 2012, Paper 844411. doi:10.1117/12.924791

[17] Elliott, S. J., and Rohlfing, J., "Multifunctional Design of Inertially-Actuated Velocity Feedback Controllers," *Journal of the Acoustics Society of America*, Vol. 131, No. 2, 2012, pp. 1150–1157. doi:10.1121/1.3672694

[18] Das, J., and Mallik, A. K., "Control of Friction Driven Oscillation by Time-Delayed State Feedback," *Journal of Sound and Vibration*, Vol. 297, Nos. 12, 2012, pp. 578–594. doi:10.1016/j.jsv.2006.04.013

[19] Fanson, J. L., and Caughey, T. K., "Positive Position Feedback Control for Large Space Structures," *AIAA Journal*, Vol. 28, No. 4, 1990, pp. 717–724. doi:10.2514/3.10451

[20] Baz, A., Poh, S., and Fedor, J., "Independent Modal Space Control with Positive Position Feedback," *Journal of Dynamic Systems Measurement and Control*, Vol. 114, No. 1, 1992, pp. 96–103. doi:10.1115/1.2896512

[21] de Marneffe, B., Avraam, M., Deraemaeker, A., Horodinca, M., and Preumont, A., "Vibration Isolation of Precision Payloads: A Six-Axis Electromagnetic Relaxation Isolator," *Journal of Guidance, Control, and Dynamics*, Vol. 32, No. 2, 2009, pp. 395–401. doi:10.2514/1.39414

[22] Mahmoodi, S. N., and Ahmadian, M., "Active Control of Structures with Adaptive Modified Positive Position Feedback," *Proceedings of the SPIE Active and Passive Smart Structures and Integrated Systems*, Vol. 7977, SPIE, Bellingham, WA, March 2011, Paper 79770E. doi:10.1117/12.880820

[23] Cohan, L. E., and Miller, D. W., "Dynamic Wavefront Control for Lightweight Mirrors in Space Telescopes," *Proceedings of the SPIE UV/Optical/IR Space Telescopes: Innovative Technologies and Concepts III Conference*, Vol. 6687, SPIE, Bellingham, WA, 2007, Paper 66870Z. doi:10.1117/12.731782

[24] Yang, F., Sedaghati, R., and Esmailzadeh, E., "Vibration Suppression of Curved Beam-Type Structures Using Optimal Multiple Tuned Mass Dampers," *Journal of Vibration and Control*, Vol. 20, No. 6, 2012, pp. 859–875. doi:10.1177/1077546312468461

[25] Diaz, I. M., and Reynolds, P., "Acceleration Feedback Control of Human-Induced Floor Vibrations," *Engineering Structures*, Vol. 32, No. 1, 2010, pp. 163–173. doi:10.1016/j.engstruct.2009.09.003

[26] Xu, Z. B., Gong, X. L., Liao, G. J., and Chen, X. M., "An Active-Damping-Compensated Magnetorheological Elastomer Adaptive Tuned Vibration Absorber," *Journal of Intelligent Material Systems and Structures*, Vol. 21, No. 10, July 2010, pp. 1039–1047. doi:10.1177/1045389X10375485

[27] Sun, H. l., Zhang, P. Q., Chen, H. B., Zhang, K., and Gong, X. L., "Application of Dynamic Vibration Absorbers in Structural Vibration Control Under Multi-Frequency Harmonic Excitations," *Applied Acoustics*, Vol. 69, No. 12, 2008, pp. 1361–1367. doi:10.1016/j.apacoust.2007.10.004

[28] Miller, D. W., Weck, O. L., and Mosier, G. E., "Framework for Multidisciplinary Integrated Modeling and Analysis of Space Telescopes," *Proceedings of the SPIE Integrated Modeling of Telescopes*, Vol. 4757, SPIE, Bellingham, WA, 2002, pp. 1–18. doi:10.1117/12.489831

[29] LoBosco, D. W., Blaurock, C., Chung, S., and Miller, D. W., "Integrated Modeling of Optical Performance for the Terrestrial Planet Finder Structurally Connected Interferometer," *Proceedings of the SPIE Modeling and Systems Engineering for Astronomy Conference*, Vol. 5497, SPIE, Bellingham, WA, 2004, pp. 278–289. doi:10.1117/12.550929

[30] Preumont, A., *Vibration Control of Achieve Structures*, 3rd ed., Springer, Berlin, 2011, pp. 137–140.

[31] Elliott, S. J., Serrand, M., and Gardonio, P., "Feedback Stability Limits for Active Isolation Systems with Reactive and Inertial Actuator," *Journal of the Acoustic Society of America*, Vol. 124, No. 2, 2008, pp. 886–897. doi:10.1115/1.1350822

[32] Hu, Q., Jia, Y. H., and Xu, S. J., "Adaptive Suppression of Linear Structural Vibration Using Control Moment Gyroscopes," *Journal of Guidance, Control, and Dynamics*, Vol. 37, No. 3, May–June 2014, pp. 990–995. doi:10.2514/62267

[33] Yang, J. F., Xu, Z. B., Wu, Q. W., Wang, Z. S., Li, H., and He, S., "Design of a Vibration Isolation System for the Space Telescope," *Journal of Guidance, Control, and Dynamics*, (to be published). doi:10.2514/1.G001221

[34] Genberg, V., Doyle, K., and Michels, G., "Optical Performance as a Function Dynamic Mechanical Loading," *Proceedings of SPIE Optical Modeling and Performance Predictions Conference*, Vol. 5178, SPIE, Bellingham, WA, Aug. 2003, pp. 14–19. doi:10.1117/12.507859

[35] Doyle, K., Genberg, V., and Michels, G., *Integrated Optomechanical Analysis*, 1st ed., SPIE, Bellingham, WA, Oct. 2002, pp. 127–144.